ATOMIC LAYER DEPOSITION
INTERNATIONAL JOURNAL

OPEN ACCESS Research Article

Transformation kinetics for low temperature post-deposition crystallization of TiO_2 thin films prepared via atomic layer deposition (ALD) from tetrakis(dimethylamino)titanium(IV) (TDMAT) and water

Jamie P. Wooding[1], Shawn A. Gregory[1], Amalie Atassi[1], Guillaume Freychet[2], Kyriaki Kalaitzidou[3,1], Mark D. Losego[1]

1 School of Materials Science and Engineering, Georgia Institute of Technology, Atlanta, GA 30332, USA
2 Energy Sciences Directorate/Photon Science Division, NSLS-II, Brookhaven National Laboratory, Upton, NY 11973, USA
3 George W. Woodruff School of Mechanical Engineering, Georgia Institute of Technology, Atlanta, GA 30332, USA
Corresponding author: Jamie P. Wooding (jwooding3@gatech.edu)

Received: 15 July 2022 **Accepted:** 24 September 2022 **Published:** 27 March 2023

Citation: Wooding JP, Gregory SA, Atassi A, Freychet G, Kalaitzidou K, Losego MD (2023) Transformation kinetics for low temperature post-deposition crystallization of TiO_2 thin films prepared via atomic layer deposition (ALD) from tetrakis(dimethylamino)titanium(IV) (TDMAT) and water. Atomic Layer Deposition 1: 1–18, https://doi.org/10.3897/aldj.1.101276

Abstract

Background: We report on the fundamental crystallization kinetics of atomic layer deposited (ALD) TiO2 thin films undergoing a post-deposition anneal (PDA) at low temperatures to probe differences in the as-deposited film microstructure.

Methods: The system of study is ALD TiO2 thin films prepared from tetrakis(dimethylamino)titanium(IV) (TDMAT) and water at 120 °C, 140 °C and 160 °C followed by ex situ low temperature annealing at temperatures ranging from 140 °C to 220 °C. All as-deposited TiO2 thin films are amorphous by X-ray diffraction (XRD). Post-deposition annealing (PDA) produces large grain anatase crystals, confirmed by XRD and top-view scanning electron microscopy (SEM). A detailed SEM study is performed to quantify the nucleation and growth kinetics by fitting microstructural data to the Johnson-Mehl-Avrami-Kolmogorov (JMAK) equation. Finally, a time-temperature-transformation (TTT) diagram is constructed to summarize the differences in crystallization behavior at different ALD deposition temperatures.

Results and conclusions: Fitting microstructural data to the JMAK equation reveals an Avrami exponent close to 3 with continuous nucleation, suggesting two-dimensional, plate-like crystal growth. Applying an Arrhenius relationship to the phase transformation data, the combined activation energy for nucleation and growth is found to be 1.40–1.58 eV atom-1. Nucleation rates are determined, and an Arrhenius relationship is used to calculate the critical Gibbs free energy for nucleation (~1.3–1.4 eV atom-1). As such, nucleation is the rate-limiting step for the amorphous to anatase phase transformation. ALD growth temperature is found to dictate film microstructure with lower deposition temperatures reducing the nucleation rate and leading to larger grain sizes irrespective of PDA conditions. The nucleation rate pre-exponential frequency factor increases with increasing deposition temperature, thereby increasing the likelihood for nucleation. Interestingly, it is this difference in the vibrational modes of the amorphous

structure, as indicated by the variation in the nucleation rate pre-exponential frequency factor, that alters the phase transformation rates and not a change in the activation energies for the transformation.

Key words: Nucleation and Growth, Microstructure, TiO2, crystal growth, anatasex-ray diffraction (XRD), Johnson-Mehl-Avrami-Kolmogorov (JMAK) equation, Thin Film growth, kinetics, phase transformation

1. Introduction

Titanium dioxide (TiO_2) is a wide-bandgap semiconductor with phase-dependent high refractive index and high dielectric constant [1, 2]. While the anatase phase is preferred for photocatalysis[3] and gas sensing,[4] rutile is preferred for high-*k* applications [5]. Amorphous TiO_2 is preferred for diffusion barriers[6] and corrosion prevention [7]. TiO_2 has also been applied in nanolaminates with Al_2O_3 in optical thin film applications,[8, 9] and with HfO_2 for increased dielectric permittivity in capacitors [10]. Many applications require uniform TiO_2 thin films that are conformal with precise thickness control [11]. Atomic layer deposition (ALD) is a well-known growth process to achieve such thin films. As such, understanding TiO_2 phase control in ALD films is important.

TiO_2-ALD has been studied extensively using $TiCl_4$ and H_2O as co-reactants [12, 13, 14]. For $TiCl_4/H_2O$ ALD chemistry, films are typically reported as being amorphous when deposited at temperatures less than 150 °C, with the onset of anatase phase crystallization around 150 °C[5, 14, 15] and rutile phase crystallization requiring temperatures of 350 °C[14] or greater [5, 16]. ALD TiO_2 films deposited from tetrakis(dimethylamino)titanium(IV) (TDMAT) and H_2O are well-studied but to a lesser extent. TDMAT can be preferred as a precursor over $TiCl_4$ due to lack of chlorine contamination in the deposited film[17, 18] and its so-called "electrically leaky TiO_2" property [19]. However, $TDMAT/H_2O$ films are nearly always amorphous as-deposited,[18, 20, 21] given that the ALD deposition temperature window is limited by TDMAT's decomposition temperature of approximately 220 °C.[22] Studies on ALD TiO_2 deposited from $TDMAT/H_2O$ report a variety of electronic properties,[7, 23] inspiring a report from Babadi *et al.* probing the gas phase reactions and ALD cycle time [24]. However, few studies exist on post-deposition crystallization of $TDMAT/H_2O$-based ALD TiO_2 thin films,[25 ,26 ,27, 28] and these studies do not go into microstructural detail at low annealing temperatures.

Crystalline as-deposited ALD films often show columnar grains through the film thickness. The grain size is typically less than the film thickness given a high density of nuclei during the initial stage of film growth [29]. However, TiO_2 ALD films grown from $TiCl_4/H_2O$ chemistry have been shown to exhibit anatase crystals greater in diameter than the film thickness [30, 31, 32]. Large-grained anatase can have improved photoelectrochemical performance[16, 33] and photocatalytic activity due to its small grain boundary volume[3, 34]. Highly defected grain boundary regions do not contribute to the functional performance of the crystalline film, and so maximizing grain size and minimizing grain boundary volume is essential to optimizing material performance. A literature review of the crystal size to TiO_2 film thickness ratio as a function of deposition temperature for $TiCl_4/H_2O$ and $TDMAT/H_2O$ ALD processes is presented in Figure 1. Reported large-grain TiO_2 processes require deposition temperatures between 200 °C and 300 °C. These reports are primarily for as-deposited films from $TiCl_4/H_2O$ chemistry on both silicon and amorphous-Al_2O_3. Here the resultant TiO_2 anatase grain size to film thickness ratio for films on amorphous-Al_2O_3[30, 32] is an order of magnitude greater than for films deposited on silicon,[15, 30, 32, 35, 36, 37] with maximum reported ratio values of 40 and 5 respectively. Large anatase crystal growth is heavily substrate[30] and surface energy[31, 38] dependent. This phenomenon has yet to be reported using $TDMAT/H_2O$ ALD; as such, in Figure 1, we highlight this work's contribution to forming large grain anatase from $TDMAT/H_2O$ chemistry by PDA.

Other reports have probed resultant ALD-TiO_2 film structure with post-deposition annealing (PDA) [5, 14, 33, 37]. PDA temperatures are typically higher than those used for the ALD growth process.

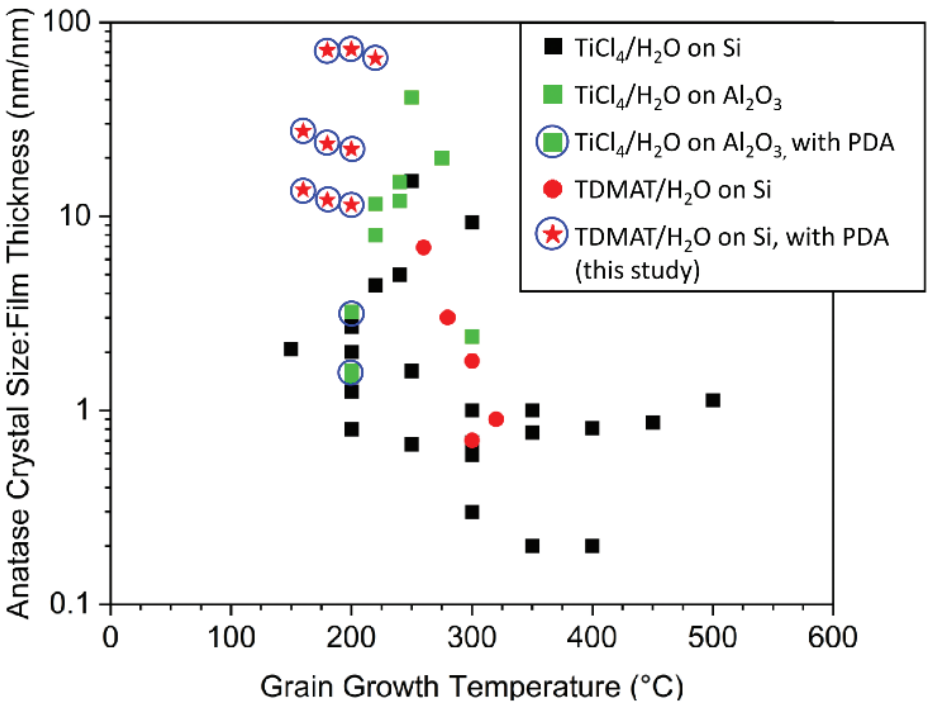

Figure 1. Plot of the crystal-size-to-film-thickness ratio as a function of the crystallization temperature compiled from various TiO2 ALD literature reports. All reports use thermal-ALD with water as the co-reactant. Varying titanium precursor and substrate chemistries are noted by data point shape as indicated in the legend. Conditions reported include: TiCl4/H2O on Si as deposited (black square), TiCl4/H2O on Al2O3 as deposited (green square), TiCl4/H2O on Al2O3 with PDA (circled green square), TDMAT/H2O on Si as deposited (red circle), and TDMAT/H2O on Si with PDA, which are the results from this study (circled red star). Films that undergo PDA are all circled in blue.

Amorphous as-deposited films are crystallized to anatase at PDA temperatures of 700 °C or lower. PDA of films at temperatures ranging from 300 to 800 °C have been reported to decrease impurity concentrations and increase crystalline phases [39]. Annealing atmosphere is also significant. Jogi *et al*. found that annealing at 750 °C in 1 atm O_2 for 10 min promoted crystallization into the anatase phase [5]. Luka *et al.* performed the most comprehensive PDA study at 160 – 220 °C on thick films (4000, 7000, and 10000 ALD cycles) in N_2 environment and proposed that anatase regions in the as-deposited film grow into the surrounding amorphous regions to transform the films during PDA. However, Aarik *et al*. found that annealing amorphous films at 400 °C in air and N_2 for 6 hours did not cause a phase transformation, attributing this to chlorine residue in the film [14]. Iancu *et al*., annealing 30 nm amorphous TiO_2 films from TDMAT/H_2O found that O_2 PDA at 700 °C and higher was more effective in forming rutile than N_2 PDA [27].

Here, we describe the first detailed study of anatase formation in TiO2 thin films deposited on a silicon wafer substrate from TDMAT/H2O thermal ALD and post-deposition annealing (PDA) in air. This study provides new information on TiO2 crystal growth during post-deposition annealing and challenges the present understanding of the temperatures required for crystallization to occur. The temperature-dependent crystallization kinetics presented are determined from an array of deposition and annealing temperatures. Using the Johnson-Mehl-Avrami-Kolmogorov (JMAK) equation, the Avrami exponent is calculated and the low-temperature anatase crystal growth mode is identified. Further, the activation energy for anatase nucleation and growth is calculated, nucleation rates are determined, and the critical Gibbs free energy for nucleation is deconvoluted from the activation energy for crystal growth. This study advances understanding of the amorphous to crystalline phase transformation in ALD TiO2 thin films and identifies how the as-deposited amorphous structure of a film can influence crystallization kinetics and final film microstructure.

2. Experimental

2.1. ALD conditions

ALD was conducted in a home-built, hot-walled, flow-tube reactor with custom LabVIEW control software [40]. Nitrogen (99.999% purity, Airgas) was used as the carrier gas at a constant flow rate of 90 sccm, resulting in a chamber pressure of 1.15 Torr. For all ALD processing, the deposition region was held, as specified, at 120 °C, 140 °C, or 160 °C and all gas process lines were maintained at 110 °C. Depositions were performed on 1 cm × 1 cm Si substrates containing their native oxide layer (WRS Materials, P/Boron<100>, 0–100 Ω). All silicon surfaces were first cleaned with a 5-minute air plasma treatment (Expanded Plasma Cleaner PDC-001, Harrick Plasma) with RF level high, to remove the adventitious carbon and leave a native oxide thickness of approximately 1.7 nm as determined by spectroscopic ellipsometry.

Tetrakis(dimethylamino)titanium(IV) (TDMAT, 99% purity) from Strem Chemicals, Inc. (Newburyport, MA, USA) and deionized water were used as the precursor and co-reactant for ALD of TiO2 films. TDMAT was dosed in a bubbler configuration with delivery lines to the reactor heated to 82 °C. Each ALD cycle used a deposition sequence of 1.0 s TDMAT / 5 s N2 purge / 0.4 s H2O / 85 s N2 purge. For all conditions, 1120 ALD cycles were deposited to yield 50 nm to 58 nm TiO2 films. ALD growth per cycle (GPC) values varied from 0.44 Å to 0.54 Å and are presented in Suppl. material 1: fig. S1a. The GPC decreased with increasing ALD temperature, which is consistent with literature reports for TDMAT/H2O thermal ALD [36, 41]. Suppl. material 1: Fig. S1b presents index of refraction, n, values measured at 550 nm for the as-deposited and annealed films. For TiO2 films deposited at each ALD temperature, annealing increased the refractive index, as expected. Refractive index values measured at 550 nm approached 2.55 after PDA, which is close to literature reported refractive index values of 2.6 for anatase [42]. As detailed in Table 1, in this work two experimental parameters were explored: (1) varying the deposition temperature between 120 °C and 160 °C and (2) varying the ex situ post deposition anneal (PDA) temperature from 140 °C to 220 °C. PDA was performed in an oven in air at atmospheric pressure. Room temperature TiO2 films on Si were placed into a pre-heated oven at the target annealing temperature. At the end of the desired anneal period, the TiO2 films were removed from the oven and passively cooled to room temperature. The TiO2 films were imaged by SEM periodically throughout the annealing process to measure the increasing percent crystallinity. Once the film achieved >95% percent crystallinity by image analysis of SEM micrographs, we defined that as “apparent full crystallinity” and stopped continuing the annealing process.

Table 1. The range of ALD temperatures (120 °C, 140 °C, and 160 °C) and subsequent PDA temperatures (140 °C to 220 °C) studied in this work.

Deposition Temperature (°C)	PDA Temperatures (°C)
120	180, 200, 220
140	140, 160, 180, 200
160	140, 160, 180, 200

2.2. Characterization

Spectroscopic ellipsometry (alpha-SE, J.A. Woollam) was used to measure film thickness and index of refraction at 550 nm. A CodyLor model was used to describe the TiO_2 layer on top of the native oxide layer on a Si substrate. Before ALD, the measured SiO_2 native oxide layer on Si was approximately 1.7 nm, determined by modeling a native oxide layer on Si in J.A. Woollam’s CompleteEASE software. Grazing incidence X-ray diffraction (GIXRD) was used to identify the crystalline phase of the deposited films. GIXRD was conducted on a PANalytical Empyrean system using Cu-Kα radiation, a BBHD source optic, and a PIXcel 2-dimensional detector. 2θ-ω scans were taken. Additionally, grazing incidence wide-angle X-ray scattering (GIWAXS) measurements were performed on a TiO_2 film set for as-deposited, short

PDA, and long PDA conditions. GIWAXS was used to verify that the initial crystal growth viewed in SEM is indeed the TiO_2 anatase crystalline phase that is measurable by GIXRD upon further transformation. Measurements were performed at the Soft Matter Interfaces Beamline at the National Synchrotron Light Source II with an incident energy of 12 keV and an incident angle of 0.15 degrees. Scattering patterns were recorded on a Pilatus 900 K–W detector, consisting of 0.172 mm square pixels, mounted at a fixed distance of 0.279 m from the sample position. The range of scattering angles was acquired by moving the detector horizontally on a fixed arc and post-processing the images using Xi CAM software (Pandolfi et al. 2018). Both the samples holder and the detector were enclosed in a vacuum chamber.

A Hitachi SU8230 field emission SEM (FE-SEM) operated at 1 kV accelerating voltage and 15–20 μA emission current was used to image microstructure and crystal growth from the secondary electron (SE) signal. In the images, amorphous regions appear dark while crystalline regions tend to appear bright. For each condition, at least two TiO_2 films were prepared and imaged, and images were taken top down at three different lateral locations on the film surface. Image analysis was performed with ImageJ to quantify the crystalline fraction transformed and to determine crystalline area density and size.

3. Results and discussion

3.1. Controlling grain size in post-deposition annealed films

Figure 2a presents SEM micrographs of as-deposited TiO_2 films compared to PDA films. As-deposited TiO_2 films appear grey in SEM. Small, white surface features, herein called nuclei, are routinely observed and mimic literature reports for very small crystals in otherwise amorphous thin films [30, 32]. Films deposited at 160 °C have a higher density of these nuclei compared to films deposited at lower temperatures. Upon post-deposition annealing (PDA) at 200 °C, films deposited at 160 °C develop a fine grain structure with average grain size of 540 nm, while films deposited at 140 °C and 120 °C develop larger grains with average sizes of 1.2 μm and 4.6 μm, respectively. Figure 2b reports representative GIXRD data for the as-deposited and PDA TiO_2 thin films, confirming that as-deposited films are amorphous and PDA films are the anatase crystalline phase. Note here that the small, white features in the amorphous film do not purport a crystalline signature in GIXRD or in the GIWAXS data collected at a synchrotron light source (Suppl. material 1: fig. S2). Nor do these small, white surface features seem to be correlated to the subsequent crystal growth; i.e., we do not observe one-to-one matching between nuclei and grains. This is unlike the report from Luka et al. that described TiO_2 anatase expansion from crystalline seeds[37] or from Macco et al. that described hydrogen-doped In_2O_3 isotropic crystal growth from a low density of embedded crystallites in a mostly amorphous film. Thus, these features may be sub-critical nuclei or not nuclei at all, but they are clearly different from prior reports.

Regardless, such large grain growth (>1 μm grain size in ~50 nm thick films) has not been observed before in ALD TiO_2 films using the TDMAT/H_2O chemistry. Further, it is surprising that the resultant microstructure varies so significantly depending on deposition temperature, with grain size decreasing from 4.6 μm to 540 nm with a 40 °C increase in temperature. To provide further insights into this crystallization process and to determine why resultant, annealed microstructure is determined by ALD temperature, we undertake a comprehensive time-dependent study of the crystalline transformation kinetics to understand the underlying activation energies.

3.2. Amorphous to crystalline transformation kinetics

Crystallization kinetics are studied over a range of ALD temperatures and post-deposition annealing (PDA) temperatures. Specifically, TiO_2 films deposited at substrate temperatures of 140 °C and 160 °C are annealed in air at 160 °C, 180 °C, and 200 °C, while TiO_2 films deposited at 120 °C are annealed in air at 180 °C, 200 °C, and 220 °C. Figure 3 presents a representative selection of micrographs used for tracking

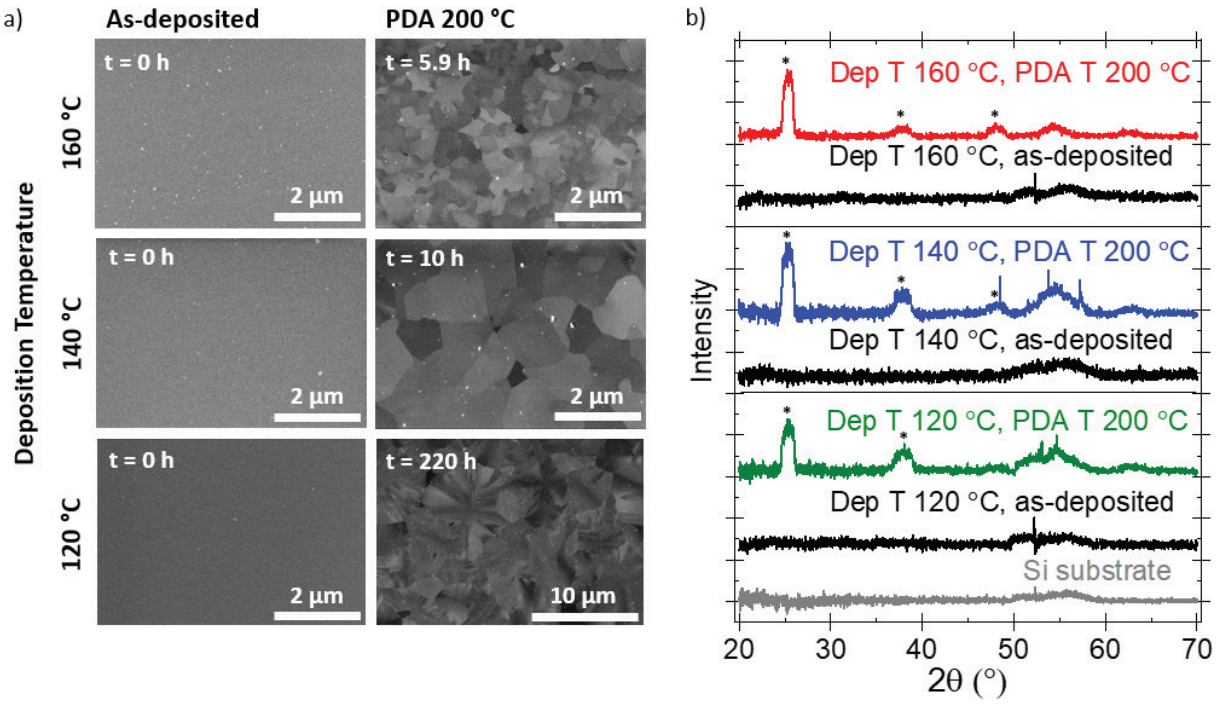

Figure 2. a) SEM micrographs for ALD films grown at 120 °C, 140 °C, and 160 °C: as-deposited (left) vs. post-deposition annealed at 200 °C in air (right). Anneal times to achieve apparent full crystallinity are listed on micrographs. Note the scale bar is different in the 120 °C PDA 200 °C micrograph to capture the large grain size. **b)** GIXRD scans for as-deposited and annealed (PDA at 200 °C in air) films deposited at 120 °C, 140 °C, and 160 °C. The three primary TiO2-anatase peaks are labeled: 2θ = 25.3°, 37.8°, 48.0°.

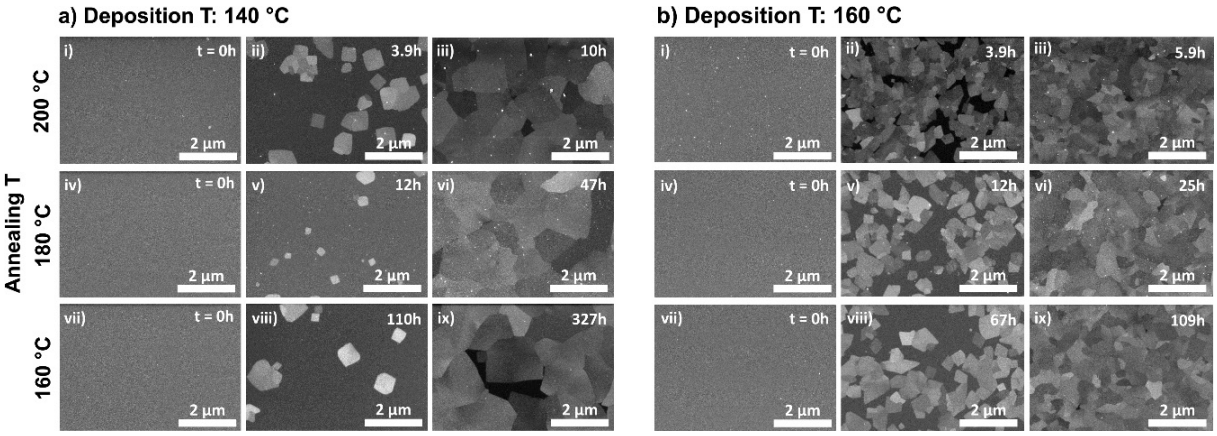

Figure 3. SEM micrographs for TiO2 films deposited at a) 140 °C and post-deposition annealed (PDA) at 200 °C for i) 0 h, ii) 3.9 h, and iii) 10 h, at 180 °C for iv) 0 h, v) 12 h, and vi) 47 h, and at 160 °C for vii) 0 h, viii) 110 h, and ix) 327 h. SEM micrographs for TiO2 films deposited at b) 160 °C and post-deposition annealed (PDA) at 200 °C for i) 0 h, ii) 3.9 h, and iii) 5.9 h, at 180 °C for iv) 0 h, v) 12 h, and vi) 25 h, and at 160 °C for vii) 0 h, viii) 67 h, and ix) 109 h. Annealing time in hours is for the specified time, t, duration.

crystal growth during PDA. Here, the brighter regions are crystalline while the darker regions are amorphous. Suppl. material 1: fig. S3 provides a representative crystal growth series for TiO_2 films deposited at 120 °C. Suppl. material 1: fig. S4 presents an SEM image and explains the ImageJ processing steps to quantify the percent crystalline phase. Figure 4a–c plots the crystalline fraction transformed determined from this image analysis for TiO_2 films deposited at 120 °C, 140 °C and 160 °C and then annealed at 160 °C, 180 °C, 200 °C, and 220 °C. These data series exhibit the expected S-curve shape and can be fit to the

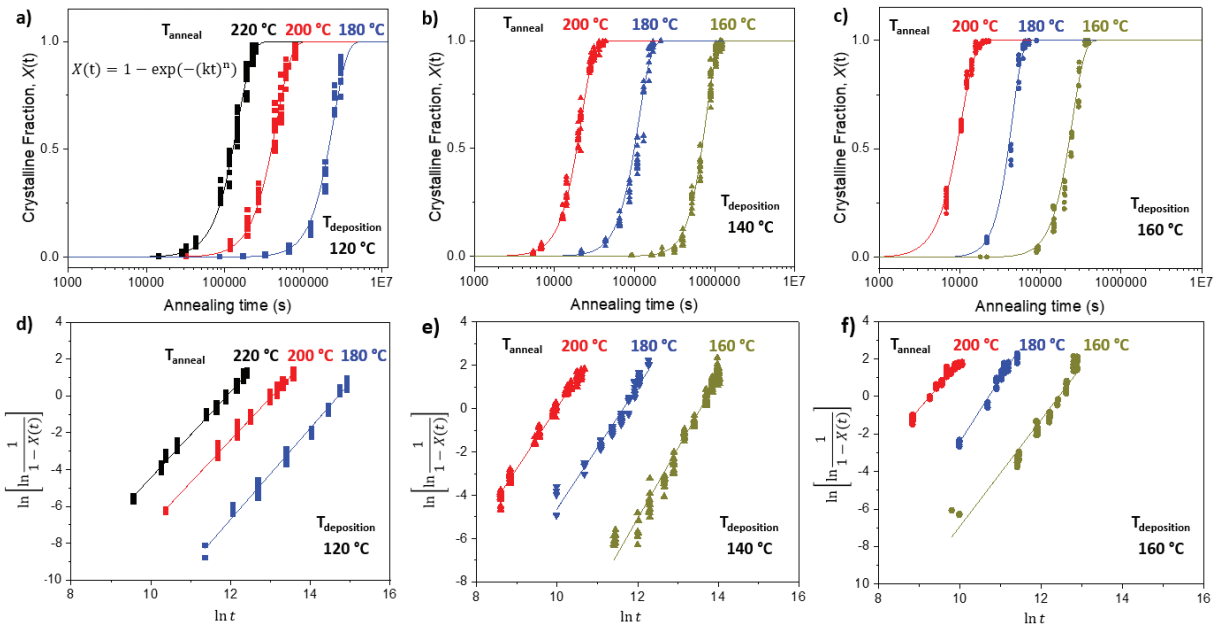

Figure 4. a) Amorphous TiO2 to anatase phase transformation curves for films deposited at (**a**) 120 °C (solid square marker), (**b**) 140 °C (solid triangle marker) and (**c**) 160 °C (solid circle marker) and post-deposition annealed at 160 °C (gold-colored), 180 °C (blue-colored), 200 °C (red-colored), and 220 °C (black-colored). The solid lines are the X(t) model fit for the calculated reaction rate k and Avrami exponent n values. Linearized form of the crystalline fraction transformation curves to extract calculated reaction rate k and Avrami exponent n values for films deposited at (**d**) 120 °C, (**e**) 140 °C, and (**f**) 160 °C.

Johnson-Mehl-Avrami-Kolmogorov (JMAK) equation[44, 45, 46]. The general form of the JMAK equation (Equation 1) is applied to model the fraction transformed to the crystalline phase $X(t)$ over PDA time t:

$$X(t) = 1 - \exp\left(-kt^n\right) \qquad \text{Equation 1}$$

Here, k is the reaction rate for combined anatase nucleation and growth and n is the Avrami exponent, which often characterizes the mechanism and dimensionality of the phase transformation. The JMAK equation as presented in Equation 1 is linearized to the following form:

$$\ln\left[\ln\frac{1}{1-X(t)}\right] = n\ln k + n\ln t \qquad \text{Equation 2}$$

In plotting $\ln\left[\ln\frac{1}{1-X(t)}\right]$ vs. ln t, the slope of this line is equal to the Avrami exponent n and the y-intercept is equal to n ln t. Applying this linearization to both deposition temperatures at each of the three PDA temperatures (Figure 4d–f), k and n are calculated for each experimentally measured transformation curve. These values are presented in Table 2.

For the complete experimental set, the values for the Avrami exponent n vary from 2.31 to 3.39, with an average value of n = 2.75. The experimental variation in n may be attributed to the nature of these *ex situ* SEM measurements: the film is removed for imaging, which causes small deviations in time and temperature associated with the cooling and re-heating of the film. The Avrami exponent should remain constant despite changes in temperature given no apparent changes in the crystal nucleation and growth mode. Given the similarity in crystalline microstructures, the crystal nucleation and growth mode at these deposition temperatures appears to be constant. The value for the Avrami exponent is dependent on the dimensionality of the product phase, the time dependence of the nucleation, and the time dependence of the rate limiting growth step. The rate-limiting growth step for an amorphous-to-crystalline transformation is the interfacial reaction. Here, nucleation appears to occur continuously with film annealing, rather than all at once. Given these condi-

Table 2. Calculated Avrami exponent n and reaction rate k for each ALD and PDA condition.

Dep T (°C)	PDA T (°C)	Avrami exponent, *n*	Reaction rate, *k*
160	200	2.51 ± 0.04	$9.6 \times 10^{-5} \pm 0.05 \times 10^{-5}$
160	180	3.39 ± 0.08	$2.2 \times 10^{-5} \pm 0.007 \times 10^{-5}$
160	160	2.85 ± 0.08	$4.0 \times 10^{-6} \pm 0.04 \times 10^{-6}$
140	200	2.80 ± 0.02	$4.6 \times 10^{-5} \pm 0.004 \times 10^{-5}$
140	180	2.82 ± 0.09	$8.8 \times 10^{-6} \pm 0.02 \times 10^{-6}$
140	160	3.25 ± 0.04	$1.3 \times 10^{-6} \pm 0.005 \times 10^{-6}$
120	220	2.34 ± 0.02	$6.8 \times 10^{-6} \pm 0.04 \times 10^{-6}$
120	200	2.31 ± 0.02	$2.2 \times 10^{-6} \pm 0.009 \times 10^{-6}$
120	180	2.49 ± 0.04	$4.1 \times 10^{-7} \pm 0.05 \times 10^{-7}$

tions, an Avrami exponent close to 3 is characteristic of a two-dimensional growth mode, indicative of plate-like microstructure observed here where there are micron-sized grains of only 50 nm thickness [47, 48, 16]. This post-deposition, *ex situ* two-dimensional grain growth is notably different than the growth mode often proposed for *in situ* TiO_2 crystal growth during an ALD process, where nucleation of some crystals occurs and growth continues vertically through the film thickness with subsequent deposition cycles [15, 29, 30].

As shown in Table 2, the combined nucleation-growth reaction rate *k* is temperature dependent, increasing with increasing PDA temperature. This result is consistent with crystalline nucleation and growth being thermally activated processes. Interestingly, at a given PDA temperature, the reaction rate *k* increases with increasing deposition temperature. This indicates that the as-deposited amorphous structures vary at the different deposition temperatures, leading to differences in the energy barriers to nucleation and/or growth. In this study, these transformational reaction rates are greater for films deposited at higher ALD temperatures. As such, transformation from the amorphous phase to the anatase phase is more favorable in amorphous TiO_2 deposited at higher temperatures.

To calculate the combined activation energy for nucleation and growth, an Arrhenius relationship [49, 50] is applied to the reaction rates *k* within a given ALD deposition temperature series as follows:

$$\mathrm{k} = k_0 * \exp\left(\frac{-E_{nuc-growth}}{k_B T_{PDA}}\right) \qquad \text{Equation 3}$$

In Equation 5, $E_{nuc\text{-}growth}$ is the activation energy for crystal nucleation and growth, k_B is the Boltzmann constant, T_{PDA} is the annealing temperature, and k_0 is a material-dependent frequency factor. The linearized form of Equation 3 is:

$$\ln(k) = \left(-\frac{-E_{nuc-growth}}{k_B}\right)\frac{1}{T_{PDA}} + \ln(k_0) \qquad \text{Equation 4}$$

Figure 5 applies the linearized form Equation 4 to make an Arrhenius plot to extract the activation energy for crystal nucleation and growth and the reaction rate frequency factor for each ALD deposition temperature. As seen in Figure 5, the activation energy for anatase phase nucleation and growth is ~1.5 eV $atom^{-1}$, which is in agreement with reported literature [37]. Surprisingly, this activation energy is independent of ALD deposition temperature; at 120 °C $E_{nuc\text{-}growth}$ = 1.46 eV $atom^{-1}$, at 140 °C $E_{nuc\text{-}growth}$ = 1.58 eV $atom^{-1}$, and at 160 °C $E_{nuc\text{-}growth}$ = 1.40 eV $atom^{-1}$. This result suggests that the change in the transformation process is the result of the pre-exponential factor, k_0. To evaluate k_0, the activation energy is set to the average value of 1.48 eV $atom^{-1}$ for all deposition temperatures and the intercepts are evaluated. The reaction rate frequency factor, k_0, is a complex factor dependent upon the vibration frequency of the atoms in the as-deposited structure. The reaction rate frequency factor increases with increasing ALD temperature: 1.1×10^{10} s^{-1} for 120 °C growth temperature, 2.5×10^{11} s^{-1} for 140 °C growth temperature, and 6.2×10^{11} s^{-1} for 160 °C growth temperature. The frequency factor order of magnitude is close to that reported in glass science crystallization kinetics literature [51] and agrees with expectations for molecular vibration.

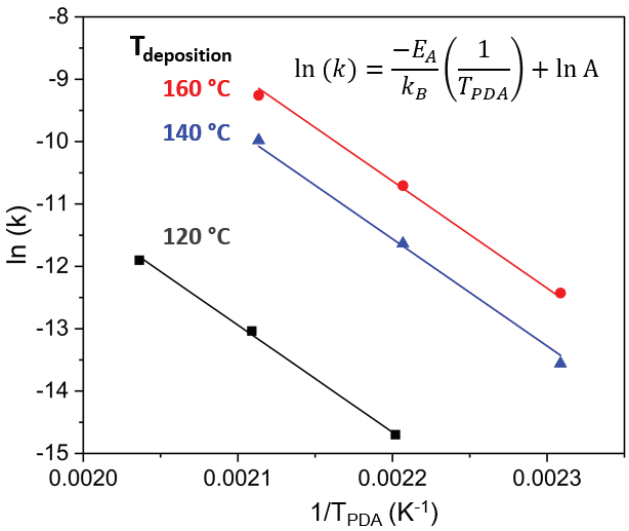

Figure 5. Arrhenius dependence for reaction rate k, relating to the combined activation energy for crystal nucleation and growth.

To better understand how anatase nucleation and growth rates vary as a function of ALD and PDA temperature, we further consider how the reaction rate *k* from the JMAK equation is defined (Equation 1). Equation 1 presents the generalized form of the JMAK equation. However, in considering a two-dimensional transforming area with continuous nucleation and growth, as is the case in this experimental work, the equation can be given as:

$$X(t) = 1 - \exp\left(-\frac{\pi}{3}\dot{N}\dot{v}^2 t^3\right) \quad \text{Equation 5}$$

Here, $\dot{N}$ is defined as the nucleation rate and $v^{\cdot}$ as the crystal growth rate. This derivation is presented in detail in Suppl. material 1: Note 1. As such, the reaction rate *k* is defined as follows:

$$k = \frac{\Delta}{3}\dot{N}\dot{v}^2 \quad \text{Equation 6}$$

Recall that the reaction rate *k* is determined experimentally from the slope equal to *n* ln *k* in the linearized JMAK equation (Equation 2). By deconvoluting the reaction rate into nucleation rate and crystal growth rate, we can separate nucleation kinetics and crystal growth kinetics.

To accomplish this deconvolution, crystal nucleation rate $\dot{N}$ is independently determined from short PDA times, prior to impingement of growing crystals. The number of crystals per area in the SEM images are counted at these short PDA times to give a nucleation rate of number of crystals m^{-2} s^{-1}. The instantaneous nucleation rate $\dot{N}$ is plotted on a log scale against PDA temperature as a function of deposition temperature in Figure 6a. For a given annealing temperature at a given deposition temperature, $\dot{N}$ is approximately constant. Nucleation rates increase by just under an order of magnitude with each 20 °C increase in PDA temperature. Films deposited at 160 °C have the greatest nucleation rates and those deposited at 120 °C have the slowest. The nucleation rate, $\dot{N}$, can be described by an Arrhenius relationship:

$$\dot{N} = N_j \exp\left(\frac{\Delta G^*_{nuc}}{k_B T_{PDA}}\right) \quad \text{Equation 7}$$

In Equation 7, ΔG^*_{nuc} is the critical Gibbs free energy for nucleation, k_B is the Boltzmann constant, *T* is the PDA temperature, and N_j is the nucleation exponential precursor. Equation 7 is linearized to:

$$\ln(\dot{N}) = \left(-\frac{\Delta G^*_{nuc}}{k_B}\right)\frac{1}{T_{PDA}} + \ln(N_j) \quad \text{Equation 8}$$

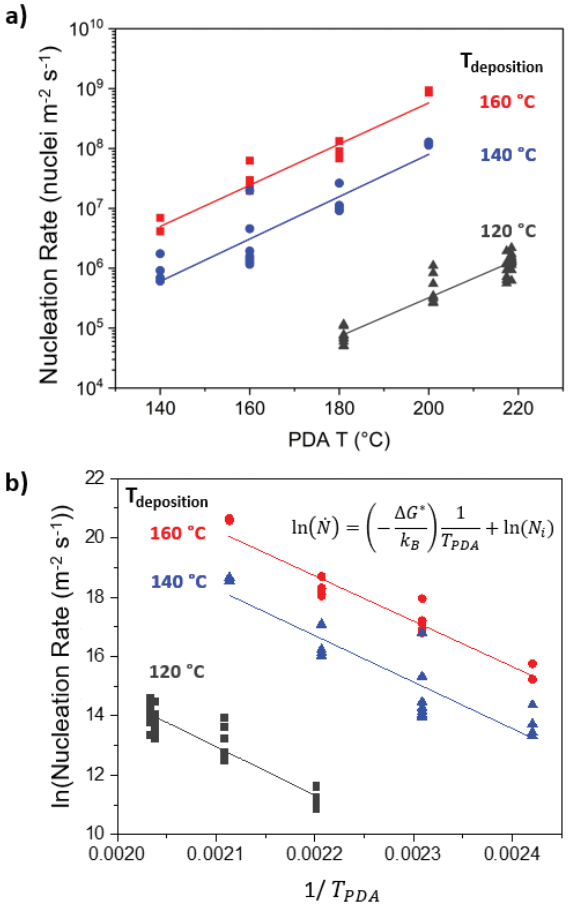

Figure 6. a) Log-linear plot of nucleation rates as a function of post-deposition annealing (PDA) temperature for ALD-TiO2 thin films deposited at 120 °C, 140 °C, and 160 °C. **b)** Linearized nucleation rate equation for films deposited at 120 °C, 140 °C, and 160 °C with linear regression line of best fit.

Here, N_j is equal to $f_{nucleation} * C_{het}$ where $f_{nucleation}$ is a frequency factor for the phase transformation and C_{het} is the concentration of heterogeneous nucleation sites per areal density. The nucleation frequency factor includes the vibrational frequency of the atoms, the area of the critical nucleus, and an activation energy for atomic migration [52]. This Arrhenius relationship is plotted in Figure 6b to calculate ΔG^*_{nuc}. As presented in Table 2, the critical free energy for nucleation, ΔG^*_{nuc}, for films deposited at 160 °C is 1.32 eV atom^{-1}, for films deposited at 140 °C is 1.35 eV atom^{-1}, and for films deposited at 120 °C is 1.41 eV atom^{-1}. Considering the error presented in Table 2, these critical free energy values for nucleation are roughly equivalent.

As seen in Figure 6b, the y-intercept $\ln(N_i)$ increases with increasing deposition temperature. Therefore, the nucleation frequency factor, $f_{nucleation}$, also increases, as with the reaction rate frequency factor, k_0. This increased nucleation frequency factor at higher deposition temperatures is consistent and designates a fundamental difference in the structure between the as-deposited ALD TiO_2 thin films. Previous studies have reported property variations in amorphous TiO_2 films as a function of ALD temperature that could be indicative of thin film structural differences. Piercy et al. found increasing density in amorphous TiO_2 from ALD temperatures 38 °C to 150 °C [53] and DeCoster et al. found thermal conductivity also increased with increasing deposition temperature for amorphous TiO_2 thin films [54]. Increasing thermal conductivity is indicative of increasing vibrational modes in the material. From the present study, an increased nucleation frequency factor indicates that there is a greater frequency of attempts to form anatase nuclei of critical size, therefore aligning with increased vibrational motion at higher deposition temperatures. This result could also inform a recent literature report that describes how increasing the ALD growth temperature from 100 to 150 °C enables the formation of high-quality,

protective anatase TiO_2 coatings at decreased annealing temperatures [33]. The amorphous TiO_2 coating deposited at 150 °C may have a higher degree of vibrational motion causing a greater number of critical nuclei formed per attempt frequency, enabling phase transformation to occur at lower temperature.

Experimentally determined values for reaction rate k and nucleation rate $\dot{N}$ are used to calculate the crystal growth rate for each deposition and annealing condition. For two-dimensional, plate-like growth, Equation 6 can be solved for crystal growth rate $\dot{v}$ as follows:

$$\dot{v} = \sqrt{\frac{3k}{\Delta \dot{N}}} \qquad \text{Equation 9}$$

Here, the reaction rate and the average nucleation rate at a given deposition temperature and annealing temperature are used to calculate each crystal growth rate. These instantaneous crystal growth rates are plotted against deposition temperature in Figure 7a. The annealing temperatures presented in Figure 7a are limited to those applicable to all three deposition temperatures and so Figure 7a only includes crystal growth rates for 180 °C and 200 °C PDA. Crystal growth rates are the highest for films deposited at 120 °C, while those for 140 °C and 160 °C films are relatively similar. The crystal growth rate is a stronger function of deposition temperature than PDA temperature.

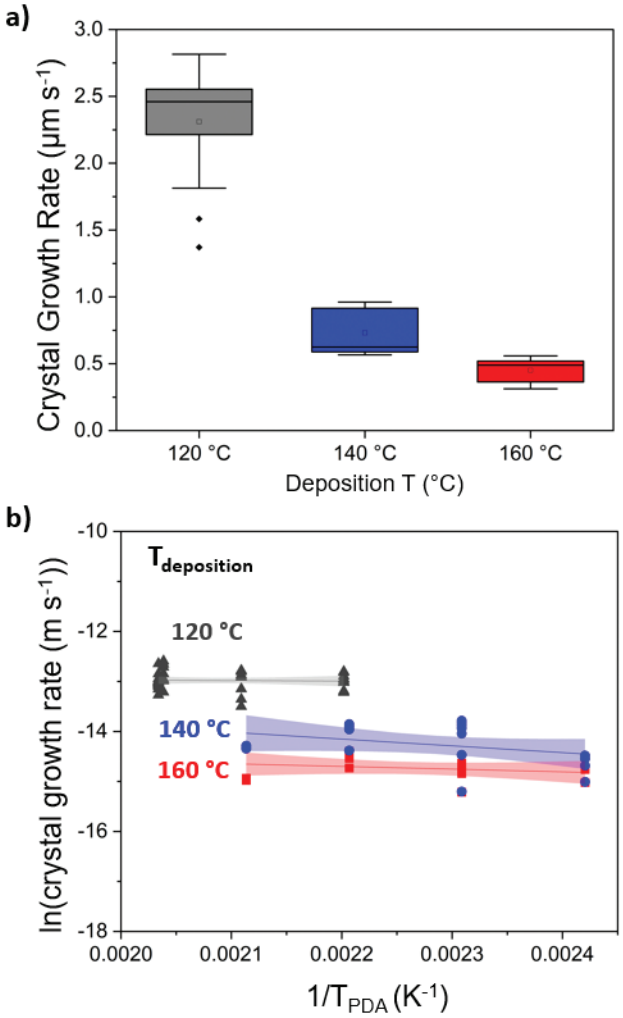

Figure 7. a) Crystal growth rates plotted as a function of deposition temperature for ALD-TiO2 films deposited at 120 °C, 140 °C, and 160 °C. **b)** Arrhenius plot for crystal growth rate for TiO2 films deposited at 120 °C, 140 °C, and 160 °C with linear regression lines of best fit and 95% confidence intervals. The R-square values for 120 °C, 140 °C, and 160 °C lines respectively are: 0.001, 0.123, and 0.056.

Next, we apply the nucleation rate analysis structure to crystal growth rate. Here, the Arrhenius relationship for crystal growth rate is given as:

$$\dot{v} = B\exp\left(\frac{-E_{\text{crystal growth}}}{k_B T_{PDA}}\right) \quad \text{Equation 10}$$

With the linearized form:

$$\ln(\dot{v}) = \left(\frac{-E_{\text{crystal growth}}}{k_B}\right)\frac{1}{T_{PDA}} + \ln(A) \quad \text{Equation 11}$$

In Equation 10 and Equation 11, k_B is the Boltzmann constant, T is the PDA temperature, and A is the exponential pre-factor. PDA temperature is used in Equation 10 and Equation 11 because that is the temperature at which the isothermal grain growth occurs. Figure 7b includes the Arrhenius plot for crystal growth rate for TiO_2 films deposited at 120 °C, 140 °C, and 160 °C with a linear regression line of best fit with $1/T_{PDA}$ as the abscissa. The reported R-square presented in the Figure 7b caption demonstrates the lack of correlation between grain growth rate and PDA temperature. To verify grain growth rate and PDA temperature are not correlated, we report the p-values for $\ln(\dot{v})$ vs. $1/T_{PDA}$ per deposition temperature. Here, the null hypothesis is that no significant correlation exists between $\ln(\dot{v})$ and $1/T_{PDA}$ per deposition temperature, such that the slope is equal to 0. If the p-value is less than the significance level α = 0.05, then the correlation is statistically significant, and the null hypothesis is rejected. However, if the p-value is greater than α, then the null hypothesis is accepted. The p-values for the correlation between ln(crystal growth rate, $\dot{v}$) and $1/T_{PDA}$ for films deposited at 120 °C, 140 °C, and 160 °C are 0.809, 0.129, and 0.379 respectively. As such, the correlation between crystal growth rate and PDA temperature for a sampling of this size and variation is not statistically significant and so the slope $-E_{crystal\ growth}/k_B$ is effectively 0. However, even if we disregard this poor correlation and proceed to calculating the activation energy for crystal growth, $E_{crystal\ growth}$, from the linear regression line of best fit, we get values of near-zero: 0.01 eV atom^{-1} at 120 °C deposition temperature, 0.1 eV atom^{-1} at 140 °C deposition temperature, and 0.05 eV atom^{-1} at 160 °C deposition temperature. Thus, we conclude that the crystal growth process is not strongly thermally activated, therefore the crystal growth rate does not vary with increasing PDA temperature. Additional statistical analysis of this crystal growth rate is included in Suppl. material 1: Note 2.

Calculated values for the critical Gibbs free energy for nucleation, ΔG^*_{nuc}, and the combined activation energy for nucleation and growth, $E_{nuc\text{-}growth}$, are reported in Table 3. Anatase nucleation has a significant energy barrier at these lower temperatures and composes most of the combined nucleation and growth activation energy barrier. In fact, the critical Gibbs free energy for nucleation is within error of the activation energy for nucleation and growth for each deposition temperature: 120 °C, 140 °C, and 160 °C. This result informs why the nucleation rates are a strong function of annealing temperature while the crystal growth rates are not. Since crystal growth rate is not found to be correlated to annealing temperature, we expect minimal activation energy for crystal growth. In contrast, the critical Gibbs free energy for nucleation is much higher and requires significant energy input for the phase transformation to occur. Thus, nucleation is the rate-limiting step for this transformation process.

Table 3. Calculated fundamental activation energies: critical Gibbs free energy for nucleation and combined nucleation-grain growth for each ALD temperature, and reaction rate frequency factor.

Deposition Temperature (°C)	ΔG^*_{nuc} (eV atom^{-1})	$E_{nuc\text{-}growth}$ (eV atom^{-1})	Reaction rate frequency factor, k_0 (s^{-1})
120	1.41 ± 0.08	1.46 ± 0.06	$1.1 \times 10^{10} \pm 0.04 \times 10^{10}$
140	1.35 ± 0.15	1.58 ± 0.03	$2.5 \times 10^{11} \pm 0.2 \times 10^{11}$
160	1.32 ± 0.10	1.40 ± 0.03	$6.2 \times 10^{11} \pm 0.3 \times 10^{11}$

3.3. Controlling microstructure

The above analysis deconvolutes the amorphous to anatase phase transformation reaction rate into separate nucleation and growth rates. We can apply this understanding of these fundamental kinetics to understand why the crystalline microstructures after PDA vary with ALD deposition temperature.

Figure 8 presents the calculated grain size, determined using the triple point method,[55] as a function of the ALD temperature and the post-deposition annealing (PDA) temperature. The grain size after annealing is a strong function of the deposition temperature, increasing almost an order of magnitude with each 20 °C decrease in deposition temperature. Since the Gibb's free energy for nucleation and the combined activation energy for nucleation and crystal growth do not change considerably with deposition temperature, the pre-exponential factors dominate the rates at which the phase transformation occurs. Because the amorphous TiO_2 films deposited at 160 °C have an order of magnitude higher reaction rate frequency factor compared to amorphous TiO_2 films deposited at 120 °C, more nucleation occurs in the film. This results in a greater nucleation density and a faster time to complete transformation. As such, films with a higher frequency factor form a greater number of crystal nuclei causing a densely packed, fine grain structure (< 1 μm), while films with a lower frequency factor form fewer crystal nuclei, resulting in a large grain structure (> 1 μm).

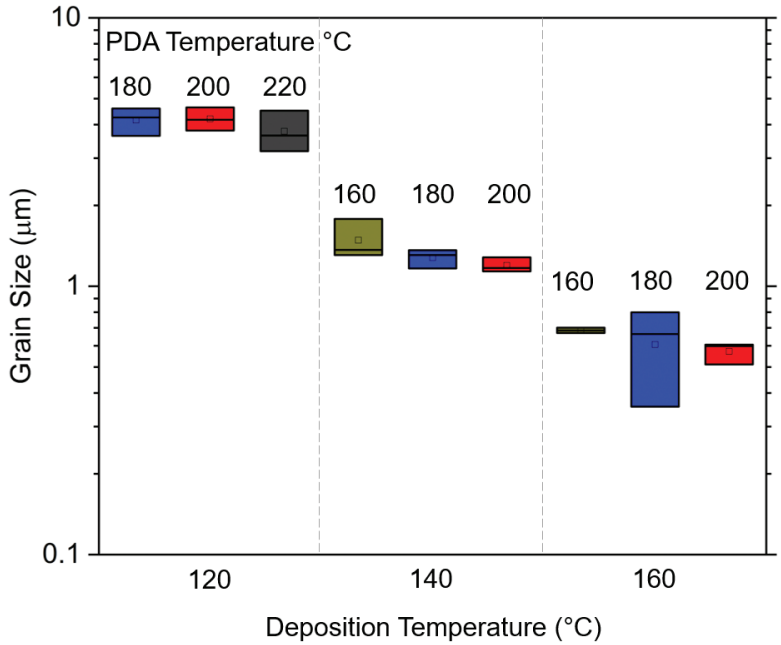

Figure 8. Calculated grain size from SEM micrograph analysis as a function of ALD temperature (120 °C, 140 °C, and 160 °C) and post-deposition annealing temperature (160 °C, 180 °C, 200 °C, 220 °C).

To discern the contribution of the crystal growth rate to final grain size, we compare the crystal size of films deposited at 160 °C and annealed at 180 °C (ALD-160 °C / PDA-180 °C) to those deposited at 140 °C and annealed at 200 °C (ALD-140 °C / PDA-200 °C). Referencing Figure 6a, the nucleation rates for these films are roughly equal, while the grain size for ALD-140 °C / PDA-200 °C films is double that of ALD-160 °C / PDA-180 °C films. This is because the crystal growth rate for ALD-140 °C films is greater than for ALD-160 °C films (Figure 7a), resulting in more rapid crystal growth that prevents as much nucleation from occurring. And since the crystal growth rate is not strongly thermally activated, for a given deposition temperature, the grain size only decreases modestly with increasing PDA temperature. So, while raising annealing temperature changes the reaction kinetics and decreases the time to transformation, it does not affect the material frequency factor and so it does not dramatically alter the final crystal microstructure.

3.4. Time-Temperature-Transformation (TTT) diagrams for plate-like anatase crystal growth

With the presented phase transformation study for TiO_2 thin films, isothermal time-temperature-transformation (TTT) diagrams can be developed to describe the TiO_2 amorphous to anatase solid-state phase transformation via post-deposition annealing (PDA). TTT diagrams can offer useful information for metal oxide thin films where the crystallization is heating-rate dependent and occurs in the solid state [56]. Figure 9 includes TTT diagrams for 5%, 50%, and 95% TiO_2-anatase transformation at ALD growth temperatures a) 120 °C, b), 140 °C, and c) 160 °C. Lower ALD temperatures suppress the amorphous to anatase phase transformation and require additional time for the transformation to occur; this is evident from the shifting in the percent crystallized curves to longer required annealing times. Higher deposition temperatures enable faster transformation to the anatase phase at each isothermal PDA temperature. These TTT diagrams for amorphous thin films crystallizing via isothermal PDA provide a guide for evaluating deposition temperature effects on the nucleation and grain growth kinetics of amorphous ALD thin films.

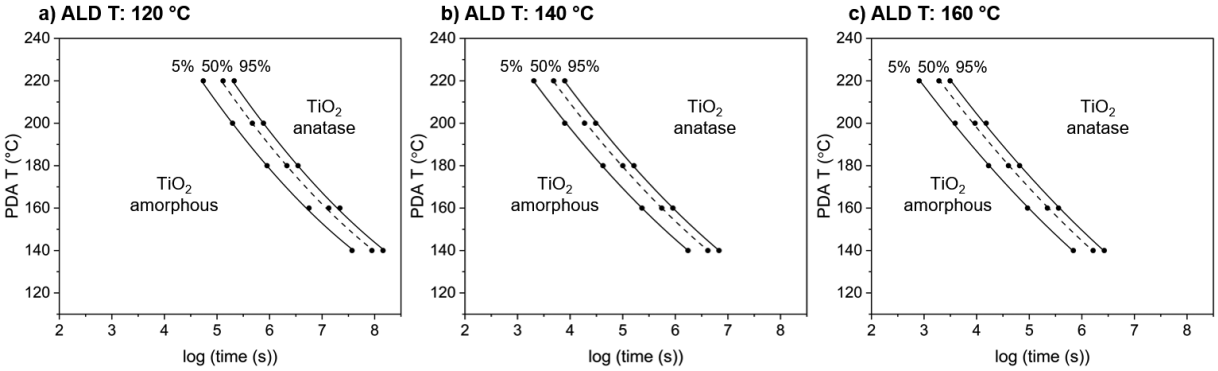

Figure 9. Time-temperature-transformation (TTT) diagrams for TiO2 amorphous to anatase phase transformation via isothermal post-deposition anneals for 1120 cycle ALD films deposited at temperatures: (**a**) 120 °C, (**b**) 140 °C, (**c**) 160 °C. Transformation curves are labeled for 5%, 50%, and 95% transformation to the TiO2-anatase phase. The abscissa axis is in base-10 log time.

4. Conclusions

We report an atomic layer deposition (ALD) process with a PDA step to grow large grain TiO_2 anatase on a Si substrate from TDMAT/H_2O chemistry. Large-grained anatase minimizes grain boundary volume and enables a greater proportion of the film to contribute its functional performance. The TiO_2-ALD is deposited from 120 °C to 160 °C with *ex situ* annealing in air from 140–220 °C. A detailed SEM study of the TiO_2-amorphous to TiO_2-anatase phase transformation is presented to extract fundamental nucleation and growth kinetics values and to highlight structural differences in the as-deposited film structure as a function of deposition temperature. The JMAK equation is used to determine an average Avrami exponent close to 3 for the transforming volume, consistent with a two-dimensional, plate-like anatase growth mode with continuous nucleation. The critical Gibbs free energy for anatase nucleation is 1.32–1.41 eV $atom^{-1}$ and the combined activation energy for nucleation and growth is 1.40–1.58 eV $atom^{-1}$, while the activation energy for crystal growth is near zero. Thus, nucleation appears to be the rate-limiting step. Interestingly, in studying the nucleation rate at different PDA temperatures as a function of ALD temperature, we identify the nucleation frequency factor, not the activation energy, as the differentiating quantity between the as-deposited TiO_2 films. Amorphous TiO_2 films deposited at higher temperatures have an increased nucleation frequency factor compared to those deposited at lower temperatures, potentially indicating that as-deposited higher temperature films have increased vibrational modes to attempt nuclei formation. As a result, ALD deposition temperature has a significant effect on the resultant grain size, with 20 °C increases in temperature decreasing the grain size by almost an order

of magnitude. Finally, a time-temperature-transformation (TTT) diagram architecture has been applied to highlight the differences in crystallization behavior between ALD temperatures.

In this work, we present a method to study differences in an as-deposited, amorphous TiO_2 film as a function of ALD deposition temperature and introduce the nucleation rate frequency factor $f_{nucleation}$ as an indicator of resultant nucleation and microstructure. Further, we separate the nucleation and growth kinetics for the amorphous to anatase phase transformation, demonstrating that nucleation is the rate-limiting step for the phase transformation under standard ALD process conditions. Finally, we demonstrate a practical low-temperature route to grow large-grained anatase films which expand their use in applications requiring temperature-sensitive substrates and devices.

Acknowledgements

J.P.W. acknowledges this material is based upon work supported by the National Science Foundation Graduate Research Fellowship under Grant No. DGE-2039655. A significant portion of this work was performed at the Georgia Tech Institute for Electronics and Nanotechnology, a member of the National Nanotechnology Coordinated Infrastructure (NNCI), which is supported by the National Science Foundation (ECCS-2025462). Any opinion, findings, and conclusions or recommendations expressed in this material are those of the authors and do not necessarily reflect the views of the National Science Foundation. The authors recognize Proposal GU-309504 for scattering measurements at Beamline 12-ID at National Synchrotron Light Source-II at Brookhaven National Lab. A.A. appreciates the support of the National Science Foundation Graduate Research Fellowship under Grant No. DGE-1650044. S.A.G. acknowledges financial support from a Link Foundation Energy Fellowship. J.P.W. thanks D. Tavakoli, T. Walters, and R. Monikandan for assistance with XRD and SEM.

References

1. Tang, H., Prasad, K., Sanjines, R., Schmid, P. & Levy, F. Electrical and optical properties of TiO_2 anatase thin films. *Journal of applied physics* 75, 2042–2047 (1994). https://doi.org/10.1063/1.356306
2. Niinistö, J., Kukli, K., Heikkilä, M., Ritala, M. & Leskelä, M. Atomic layer deposition of high-k oxides of the group 4 metals for memory applications. *Advanced Engineering Materials* 11, 223–234 (2009). https://doi.org/10.1002/adem.200800316
3. Badovinac, I. J. *et al.* Grain size effect on photocatalytic activity of TiO2 thin films grown by atomic layer deposition. *Thin Solid Films* 709, 138215 (2020). https://doi.org/10.1016/j.tsf.2020.138215
4. Dutta, P. K. *et al.* Interaction of carbon monoxide with anatase surfaces at high temperatures: optimization of a carbon monoxide sensor. *The Journal of Physical Chemistry B* 103, 4412–4422 (1999). https://doi.org/10.1021/jp9844718
5. Jõgi, I. *et al.* Conformity and structure of titanium oxide films grown by atomic layer deposition on silicon substrates. *Thin Solid Films* 516, 4855–4862 (2008). https://doi.org/10.1016/j.tsf.2007.09.008
6. Tian, H., Schryvers, D., Liu, D., Jiang, Q. & Van Humbeeck, J. Stability of Ni in nitinol oxide surfaces. *Acta Biomaterialia* 7, 892–899 (2011). https://doi.org/10.1016/j.actbio.2010.09.009
7. Hu, S. *et al.* Amorphous TiO2 coatings stabilize Si, GaAs, and GaP photoanodes for efficient water oxidation. *Science* 344, 1005–1009 (2014). https://doi.org/10.1126/science.1251428
8. Zaitsu, S.-i., Jitsuno, T., Nakatsuka, M., Yamanaka, T. & Motokoshi, S. Optical thin films consisting of nanoscale laminated layers. *Applied physics letters* 80, 2442–2444 (2002). https://doi.org/10.1063/1.1467622
9. Ylivaara, O. M. *et al.* Aluminum oxide/titanium dioxide nanolaminates grown by atomic layer deposition: Growth and mechanical properties. *Journal of Vacuum Science & Technology A: Vacuum, Surfaces, and Films* 35, 01B105 (2017). https://doi.org/10.1116/1.4966198
10. Kukli, K. *et al.* Influence of TiO2 incorporation in HfO2 and Al2O3 based capacitor dielectrics. *Thin solid films* 515, 6447–6451 (2007). https://doi.org/10.1016/j.tsf.2006.11.049

11. Ritala, M. & Leskelä, M. Atomic layer epitaxy-a valuable tool for nanotechnology? *Nanotechnology* 10, 19 (1999). https://doi.org/10.1088/0957-4484/10/1/005
12. Ritala, M., Leskelä, M., Nykänen, E., Soininen, P. & Niinistö, L. Growth of titanium dioxide thin films by atomic layer epitaxy. *Thin Solid Films* 225, 288–295 (1993). https://doi.org/10.1016/0040-6090(93)90172-L
13. Aarik, J., Aidla, A., Mändar, H. & Uustare, T. Atomic layer deposition of titanium dioxide from TiCl4 and H2O: investigation of growth mechanism. *Applied Surface Science* 172, 148–158 (2001). https://doi.org/10.1016/S0169-4332(00)00842-4
14. Aarik, J., Aidla, A., Uustare, T. & Sammelselg, V. Morphology and structure of TiO2 thin films grown by atomic layer deposition. *Journal of Crystal Growth* 148, 268–275, (1995). https://doi.org/10.1016/0022-0248(94)00874-4
15. Lee, W.-J. & Hon, M.-H. Space-Limited Crystal Growth Mechanism of TiO2 Films by Atomic Layer Deposition. *The Journal of Physical Chemistry C* 114, 6917–6921, (2010). https://doi.org/10.1021/jp911210q
16. Cheng, H.-E. & Chen, C.-C. Morphological and photoelectrochemical properties of ALD TiO2 films. *Journal of the electrochemical society* 155, D604 (2008). https://doi.org/10.1149/1.2952659
17. Xie, Q. *et al.* Atomic layer deposition of TiO2 from tetrakis-dimethyl-amido titanium or Ti isopropoxide precursors and H2O. *Journal of Applied Physics* 102, 083521, (2007). https://doi.org/10.1063/1.2798384
18. Lim, G. T. & Kim, D.-H. Characteristics of TiOx films prepared by chemical vapor deposition using tetrakis-dimethyl-amido-titanium and water. *Thin Solid Films* 498, 254–258, (2006). https://doi.org/10.1016/j.tsf.2005.07.121
19. Nunez, P. *et al.* Characterization of electronic transport through amorphous TiO2 produced by atomic layer deposition. *The Journal of Physical Chemistry C* 123, 20116–20129 (2019). https://doi.org/10.1021/acs.jpcc.9b04434
20. Xie, Q. *et al.* Growth kinetics and crystallization behavior of TiO2 films prepared by plasma enhanced atomic layer deposition. *Journal of The Electrochemical Society* 155, H688 (2008). https://doi.org/10.1149/1.2955724
21. Wachnicki, L., Gieraltowska, S., Witkowski, B. S., Godlewski, M. & Guziewicz, E. Growth and characterization of Ti-based films obtained from two selected precursors: H2O, TiCl4, Ti (N (CH3) 2) 4 or Al2 (CH3) 6 by the ALD method. *Materials Science in Semiconductor Processing* 148, 106792 (2022). https://doi.org/10.1016/j.mssp.2022.106792
22. Norton, E. T. & Amato-Wierda, C. Kinetic and mechanistic studies of the thermal decomposition of Ti (N (CH3) 2) 4 during chemical vapor deposition by in situ molecular beam mass spectrometry. *Chemistry of materials* 13, 4655–4660 (2001). https://doi.org/10.1021/cm0104708
23. Scheuermann, A. G. *et al.* Titanium oxide crystallization and interface defect passivation for high performance insulator-protected schottky junction MIS photoanodes. *ACS applied materials & interfaces* 8, 14596–14603 (2016). https://doi.org/10.1021/acsami.6b03688
24. Babadi, A. S., Tang-Kong, R. & McIntyre, P. C. Link between Gas Phase Reaction Chemistry and the Electronic Conductivity of Atomic Layer Deposited Titanium Oxide Thin Films. *J Phys Chem Lett*, 3625–3632, (2021). https://doi.org/10.1021/acs.jpclett.1c00115
25. Nabatame, T. *et al.* Electrical properties of anatase TiO2 films by atomic layer deposition and low annealing temperature. *Journal of Vacuum Science & Technology B, Nanotechnology and Microelectronics: Materials, Processing, Measurement, and Phenomena* 32, 03D121 (2014). https://doi.org/10.1116/1.4869059
26. Huang, Y., Pandraud, G. & Sarro, P. M. Characterization of low temperature deposited atomic layer deposition TiO2 for MEMS applications. *Journal of Vacuum Science & Technology A: Vacuum, Surfaces, and Films* 31, 01A148 (2013). https://doi.org/10.1116/1.4772664
27. Iancu, A. T., Logar, M., Park, J. & Prinz, F. B. Atomic layer deposition of undoped TiO2 exhibiting p-type conductivity. *ACS applied materials & interfaces* 7, 5134–5140 (2015). https://doi.org/10.1021/am5072223
28. Saari, J. *et al.* Low-Temperature Route to Direct Amorphous to Rutile Crystallization of TiO2 Thin Films Grown by Atomic Layer Deposition. *The Journal of Physical Chemistry C*, (2022). https://doi.org/10.1021/acs.jpcc.2c04905
29. Miikkulainen, V., Leskelä, M., Ritala, M. & Puurunen, R. L. Crystallinity of inorganic films grown by atomic layer deposition: Overview and general trends. *Journal of Applied Physics* 113, 021301, (2013). https://doi.org/10.1063/1.4757907
30. Puurunen, R. L. *et al.* Controlling the crystallinity and roughness of atomic layer deposited titanium dioxide films. *Journal of nanoscience and nanotechnology* 11, 8101–8107 (2011). https://doi.org/10.1166/jnn.2011.5060

31. Cho, C. J. *et al.* Interface engineering for extremely large grains in explosively crystallized TiO2 films grown by low-temperature atomic layer deposition. *Chemistry of Materials* 29, 2046–2054 (2017). https://doi.org/10.1021/acs.chemmater.6b04090
32. Piltaver, I. K. *et al.* Controlling the grain size of polycrystalline TiO2 films grown by atomic layer deposition. *Applied Surface Science* 419, 564–572 (2017). https://doi.org/10.1016/j.apsusc.2017.04.146
33. Saari, J. *et al.* Interface Engineering of TiO2 Photoelectrode Coatings Grown by Atomic Layer Deposition on Silicon. *ACS omega* 6, 27501–27509 (2021). https://doi.org/10.1021/acsomega.1c04478
34. Lee, J. *et al.* Effect of crystal structure and grain size on photo-catalytic activities of remote-plasma atomic layer deposited titanium oxide thin film. *ECS Journal of Solid State Science and Technology* 1, Q63 (2012). https://doi.org/10.1149/2.001204jss
35. Mitchell, D. *et al.* Atomic layer deposition of TiO2 and Al2O3 thin films and nanolaminates. *Smart materials and structures* 15, S57 (2005). https://doi.org/10.1088/0964-1726/15/1/010
36. Abendroth, B. *et al.* Atomic layer deposition of TiO2 from tetrakis(dimethylamino)titanium and H2O. *Thin Solid Films* 545, 176–182, (2013). https://doi.org/10.1016/j.tsf.2013.07.076
37. Luka, G. *et al.* Kinetics of anatase phase formation in TiO 2 films during atomic layer deposition and post-deposition annealing. *CrystEngComm* 15, 9949–9954 (2013). https://doi.org/10.1039/c3ce40893k
38. Dendooven, J. *et al.* In Situ X-ray Fluorescence Measurements During Atomic Layer Deposition: Nucleation and Growth of TiO2 on Planar Substrates and in Nanoporous Films. *The Journal of Physical Chemistry C* 115, 6605–6610, (2011). https://doi.org/10.1021/jp111314b
39. Niilisk, A. *et al.* Structural study of TiO2 thin films by micro-Raman spectroscopy. *Open Physics* 4, 105–116 (2006). https://doi.org/10.1007/s11534-005-0009-3
40. Piercy, B. D. & Losego, M. D. Tree-based control software for multilevel sequencing in thin film deposition applications. *Journal of Vacuum Science & Technology B* 33, 043201, (2015). https://doi.org/10.1116/1.4926676
41. Dufond, M. E. *et al.* Quantifying the Extent of Ligand Incorporation and the Effect on Properties of TiO2 Thin Films Grown by Atomic Layer Deposition Using an Alkoxide or an Alkylamide. *Chemistry of Materials* 32, 1393–1407 (2020). https://doi.org/10.1021/acs.chemmater.9b03621
42. Saha, D. *et al.* Spectroscopic ellipsometry characterization of amorphous and crystalline TiO2 thin films grown by atomic layer deposition at different temperatures. *Applied surface science* 315, 116–123 (2014). https://doi.org/10.1016/j.apsusc.2014.07.098
43. Pandolfi, R. J. *et al.* Xi-cam: a versatile interface for data visualization and analysis. *Journal of synchrotron radiation* 25, 1261–1270 (2018). https://doi.org/10.1107/S1600577518005787
44. Avrami, M. Kinetics of phase change. I General theory. *The Journal of chemical physics* 7, 1103–1112 (1939). https://doi.org/10.1063/1.1750380
45. William, J. & Mehl, R. Reaction kinetics in processes of nucleation and growth. *Trans. Metall. Soc. AIME* 135, 416–442 (1939).
46. Avrami, M. Kinetics of phase change. II transformation-time relations for random distribution of nuclei. *The Journal of chemical physics* 8, 212–224 (1940). https://doi.org/10.1063/1.1750631
47. Moghadam, M. & Voorhees, P. W. Thin film phase transformation kinetics: From theory to experiment. *Scripta Materialia* 124, 164–168 (2016). https://doi.org/10.1016/j.scriptamat.2016.07.010
48. Gutzow, I. & Schmelzer, J. *The vitreous state*. (Springer, 1995). https://doi.org/10.1007/978-3-662-03187-2
49. Arrhenius, S. Über die Reaktionsgeschwindigkeit bei der Inversion von Rohrzucker durch Säuren. *Zeitschrift für physikalische Chemie* 4, 226–248 (1889). https://doi.org/10.1515/zpch-1889-0416
50. Laidler, K. J. The development of the Arrhenius equation. *Journal of chemical Education* 61, 494 (1984). https://doi.org/10.1021/ed061p494
51. Cheng, K. Evaluation of crystallization kinetics of glasses by non-isothermal analysis. *Journal of materials science* 36, 1043–1048 (2001). https://doi.org/10.1023/A:1004804730399
52. Porter, D. A. & Easterling, K. E. *Phase transformations in metals and alloys (revised reprint)*. (CRC press, 2009). https://doi.org/10.1201/9781439883570

53. Piercy, B. D., Leng, C. Z. & Losego, M. D. Variation in the density, optical polarizabilities, and crystallinity of TiO2 thin films deposited via atomic layer deposition from 38 to 150 °C using the titanium tetrachloride-water reaction. *Journal of Vacuum Science & Technology A* 35, 03E107, (2017). https://doi.org/10.1116/1.4979047
54. DeCoster, M. E. *et al.* Density and size effects on the thermal conductivity of atomic layer deposited TiO2 and Al2O3 thin films. *Thin Solid Films* 650, 71–77 (2018). https://doi.org/10.1016/j.tsf.2018.01.058
55. Vander Voort, G. F. *Grain size measurement*. 85–131 (American Society for Testing and Materials, 1984). https://doi.org/10.1520/STP30216S
56. Rupp, J. L., Scherrer, B., Schäuble, N. & Gauckler, L. J. Time–temperature–transformation (TTT) diagrams for crystallization of metal oxide thin films. *Advanced Functional Materials* 20, 2807–2814 (2010). https://doi.org/10.1002/adfm.201000377

E-mail and ORCID

Jamie P. Wooding (Corresponding author, jwooding3@gatech.edu)
Shawn A. Gregory (shawngregory@gatech.edu), ORCID: https://orcid.org/0000-0002-1027-0675
Amalie Atassi (aatassi3@gatech.edu), ORCID: https://orcid.org/0000-0003-3218-680X
Guillaume Freychet (gfreychet@gmail.com), ORCID: https://orcid.org/0000-0001-8406-798X
Kyriaki Kalaitzidou (kyriaki.kalaitzidou@me.gatech.edu)
Mark D. Losego (losego@gatech.edu), ORCID: https://orcid.org/0000-0002-9810-9834

Supplementary material 1

Additional information

Authors: Jamie P. Wooding, Shawn A. Gregory, Amalie Atassi, Guillaume Freychet, Kyriaki Kalaitzidou, Mark D. Losego

Data type: figures and tables (PDF file)

Explanation note: fig. S1. a) ALD growth per cycle (GPC) from 1120 TDMAT/H2O cycles for asdeposited TiO2 thin films at ALD temperatures: 120 °C, 140 °C, and 160 °C. b) Index of refraction, n, measured at 550 nm for as-deposited and post-deposition anneal TiO2 thin films at ALD temperatures: 120 °C, 140 °C, and 160 °C; fig. S2. a) GIWAXS scans for films deposited at 140 °C: as-deposited, PDA at 200 °C for 2 h, and PDA at 200 °C for greater than 95% X(t) transformed. b) GIWAXS scans for films deposited at 160 °C: as-deposited, PDA at 200 °C for 1 h, and PDA at 200 °C for greater than 95% X(t) transformed; fig. S3. SEM image grid for TiO2 films deposited at 120 °C and annealed at 180 °C, 200 °C, and 220 °C for the specified time duration; fig. S4. a) Original SEM image and b) image after processing: auto contrast/brightness, despeckle, threshold, area count. In c) dark regions are crystalline, white regions are amorphous. Note 1: Derivation for JMAK equation to describe a two-dimensional transforming area with continuous nucleation and growth. Note 2: Statistical analysis for Arrhenius relationships presented in this report. tables S1, S2. For each dataset, reported Pearson's r value, critical values, and whether the correlation is statistically significant.

Link: https://doi.org/10.3897/aldj.1.101276.suppl1